PAPER

Check for updates

A core–shell MnO$_2$@Au nanofiber network as a high-performance flexible transparent supercapacitor electrode†

Soram Bobby Singh,[a] Thangjam Ibomcha Singh,[a] Nam Hoon Kim [ID] *[a] and Joong Hee Lee [ID] *[ab]

Metal oxides have attracted great attention as active materials for supercapacitor devices because of their high energy densities. However, their application for transparent supercapacitors is limited due to their opaqueness. The challenge remains to fabricate flexible transparent metal oxide supercapacitor electrodes. Here, in this paper, we report a novel technique to fabricate flexible transparent core–shell MnO$_2$@AuNF network electrodes for flexible transparent supercapacitors. A high electro-optical performance AuNF network electrode (sheet resistance 9.58 Ω sq^{-1} and optical transparency ∼93.13%) was fabricated using a scalable electrospinning process and thermal vacuum deposition technique. With the AuNF network electrode as a current collector, a hierarchal MnO$_2$ nanosheet was electrodeposited over the AuNF network, yielding a highly interconnected core–shell MnO$_2$@AuNF network electrode structure with high transparency (∼86%). The fabricated MnO$_2$@AuNF network electrode exhibited a high areal capacitance of 8.26 mF cm^{-2} at 5 mV s^{-1}, along with high rate capability, long-term cycling stability, and excellent mechanical flexibility. Furthermore, the assembled flexible transparent supercapacitor device also showed high transparency (∼79%), a high energy density of 0.14 μW h cm^{-2} at a power density of 4 μW cm^{-2}, along with excellent mechanical flexibility.

Introduction

Flexible transparent electrodes are envisioned to have a substantial impact on the development of our future smart flexible transparent optoelectronic gadgets, and other novel enhanced reality devices, as well as aesthetic household objects.[1–6] However, to produce a flexible transparent optoelectronic device, the development of primary portable power sources with mechanical flexibility, as well as long lifetime with high transparency is greatly needed. Among the flexible transparent primary portable power sources, many researchers have turned their attention to flexible transparent supercapacitors because of their excellent specific capacitance, high power density, cycle stability, and low cost.[7–12] However, to get a high-performance flexible transparent supercapacitor, the active electrode material should not only possess excellent electrochemical performance but also excellent electrical and optical properties, along with mechanical flexibility. Principally,

transparent supercapacitor electrodes should act both as current collectors, and as active materials to store electrochemical energy.[13–17] This is quite challenging as most of the active electrode materials are opaque in nature. Several flexible transparent supercapacitor devices have been demonstrated using carbon-based active electrode materials such as graphene,[10,18] carbon nanotubes (CNTs)[19–21] and conducting polymer films.[12,22,23] However, the transparency and capacitance of such flexible transparent supercapacitors depend on the thickness of the active materials.[10,22,24] For instance, Tao Cheng *et al.* reported the fabrication of a flexible transparent supercapacitor with free-standing PEDOT:PSS electrodes which yielded 65% transparency with an areal capacitance of 1.18 mF cm^{-2}, which decreased to 0.23 mF cm^{-2} with a decreasing thickness of the PEDOT:PSS layer, although the transparency of the device improved.[25] Thus, the performance of the transparent supercapacitor device seems to be a trade-off between the capacitance and transparency of the device. Significant efforts have been put forth to improve the performance of such flexible transparent supercapacitors by incorporating the flexible transparent electrode as a current collector such as metallic fabrics/graphene,[26] metal nanowires/PEDOT:PSS,[27] metal grids/PEDOT:PSS,[11,25,28] and metal NWs/polymer.[29] Although the performance of these devices was improved up to a certain extent but remains a challenge to improve transparency as well as capacitance for practical applications. In addition, the

[a]Advanced Materials Institute of BIN Convergence Technology (BK21 Plus Global), Department of BIN Convergence Technology, Chonbuk National University, Jeonju, Jeonbuk, 54896, Republic of Korea. E-mail: jhl@chonbuk.ac.kr; nhk@chonbuk.ac.kr
[b]Carbon Composite Research Centre, Department of Polymer-Nano Science and Technology, Chonbuk National University, Jeonju, Jeonbuk 54896, Republic of Korea
† Electronic supplementary information (ESI) available. See DOI: 10.1039/c9ta00778d

electrochemical performance of these materials, defined by electric double-layer capacitance, is far below the pseudo-capacitive materials such as MnO_2 which has a very high theoretical specific capacitance of 1370 F g^{-1}, nearly 1 order higher than the value of CNTs.[30] Therefore, current research has focused on the development of a flexible transparent supercapacitor device by incorporating flexible transparent current collectors with a thin layer of pseudo-capacitive materials.[15,31–34] Among the various pseudo-capacitive electrode materials for a flexible supercapacitor device, MnO_2 has been extensively studied because of its high theoretical specific capacitance, low cost, natural abundance, and environmental friendliness.[35,36] However, the application of metal oxide films for a flexible transparent supercapacitor electrode is limited due to its low electrical conductivity (10^{-5} to 10^{-6} S cm^{-1}), opaqueness and mechanically brittle nature.[37] In recent years, various strategies have been proposed to improve the conductivity as well as the capacitance of the MnO_2 by doping various elements to form an oxide matrix or forming a composite structure by combining with excellent conducting materials or developing hierarchical nanostructures.[38–40] Direct growth technique of the metal oxides on the metal network transparent electrodes using electro-chemical deposition technique has recently been demonstrated and presented more promising future supercapacitor electrodes, with high electro-optics, high electrochemical performance and good mechanical flexibility.[17,31–33] For example, S. Kiruthika et al. reported the fabrication of a high-performance flexible supercapacitor with an Au/MnO_2 electrode which yielded 75% transparency and 3 mF cm^{-2} areal capacitance, using a cracked template structure.[33] In another, T. Qiu et al. had also reported Au@MnO_2 core–shell nanomesh electrodes using nanosphere lithography combined with electro-deposition technique with an areal capacitance of 4.72 mF cm^{-2} at 48% transparency.[31] However, the reported metal network-based electrode fabrication processes were either complicated or hazardous to the environment.[11,28,33] Also, the metallic network fabricated from crack templates/polymeric nanomesh structures always suffers from a low electro-optical performance because of the large crack width size ~10 μm and dense close-packed template polystyrene (PS) particles ~700 nm,[31,33] which limits the high optical performance of the supercapacitor device. Also, environmental and eco-friendly processes are other priorities for future generations. Hence, the development of an eco-friendly high performance flexible transparent electrode is essential to produce a highly transparent flexible supercapacitor device. Recently, an electrospun based metal nanofiber network electrode has emerged as a promising flexible transparent electrode because of its high electro-optical performance.[41–44] An et al. demonstrated the best ever electro-optical performance with a sheet resistance of 0.36 Ω sq^{-1} at ~90% transmittance, based on an electrospun nanofiber using an electroplating technique.[45] So, owing to its high electro-optical performance, along with excellent mechanical properties, electrospun-based metal nanofiber network electrodes could be the best alternative for fabrication of high performance flexible transparent supercapacitor electrodes, along with an eco-friendly fabrication process. Again, the direct growth of active metal oxide films over the highly conductive metal nanofiber network by a selective electrodeposition technique might offer high electro-optical performance along with high electrochemical and mechanical properties.

Here, we propose an eco-friendly, scalable technique to fabricate a core–shell MnO_2@AuNF network structure as a high performance flexible transparent supercapacitor electrode with controllable electro-optical and electrochemical properties. With the ability to coat thin metal films using a physical deposition method, first, we made a 100 nm thin gold (Au) coated PVA nanofiber network electrode structure (AuNF network) using a scalable electrospinning process. The AuNF network possesses not only excellent electro-optical performance (sheet resistance 9.58 Ω sq^{-1} and optical transparency ~93.13%) but also good mechanical flexibility. Significantly, the highly conducting interconnected AuNF network electrode provides a podium for electrodeposition of hierarchal MnO_2 nanosheets over the AuNF network, yielding a highly interconnected core–shell MnO_2@AuNF network supercapacitor electrode structure with high transparency (~86%). The core–shell MnO_2@AuNF network supercapacitor electrode showed a high areal capacitance of 8.26 mF cm^{-2} at 5 mV s^{-1}, along with high rate capability, long-term cycling stability, and excellent mechanical flexibility. Furthermore, the fabricated solid-state supercapacitor device also showed high transparency (~79%), and high energy density, along with excellent mechanical flexibility. Thus, the electrospun-based metal nanofiber network electrode might provide a transparent electrode for the fabrication of flexible transparent supercapacitors for transparent portable electronic systems.

Experimental

Fabrication of the AuNF network electrode

A free-standing gold-coated PVA nanofiber (AuNF) network was first obtained, using electrospinning and thermal vacuum deposition techniques pioneered in the laboratory.[46] The preparation of the precursor polymer solution and electrospinning process for obtaining the free-standing PVA nanofiber web were performed similarly to our earlier reported work.[46] After that, a thin layer of gold (Au) ~100 nm is deposited on one side of the PVA nanofiber network, and then, Au is again coated on the other side of the PVA nanofiber to obtain a fully coated free standing Au nanofiber network structure, at a base pressure of 1 × 10^{-6} torr, and a deposition rate of 0.2 Å s^{-1} (E-Beam Evaporator System, BSVAC Bosung Vacuum).

Fabrication of the core–shell MnO_2@AuNF network electrode

The core–shell MnO_2@AuNF network electrode was fabricated by a potentiostatic (PS) electrodeposition technique. Typically, the electrodeposition solution contains 50 mM sodium sulfate (Na_2SO_4) and 50 mM manganese acetate (Mn(CH_3COO)$_2$). All depositions were carried out at room temperature with a three-electrode set-up, where the AuNF network electrode, Pt rod, and the Ag/AgCl electrode were used as the working, counter, and reference electrodes, respectively. Potentiostatic (PS) electrodeposition was carried out by applying a voltage of +0.6 V versus

This journal is © The Royal Society of Chemistry 2019

J. Mater. Chem. A, 2019, 7, 10672–10683 | 10673

the Ag/AgCl electrode for different electrodeposition times (1 to 30 min). After deposition, the MnO$_2$@AuNF network electrode was thoroughly washed with deionized water to remove any residual electrolyte and dried at 40 °C for 12 h in an oven.

Fabrication of flexible transparent solid-state supercapacitors

A symmetric flexible transparent solid-state supercapacitor device was fabricated using a transparent lithium chloride (LiCl)–polyvinylalcohol (PVA) gel as an electrolyte as well as a spacer. In the process, the LiCl–PVA gel electrolyte was simply prepared as follow: 2 g of PVA was first dissolved into 20 ml of deionized water at 85 °C for 2 h followed by addition of 2 g of LiCl to the PVA polymer solution under continuous stirring until a clear solution was obtained and then, cooled to room temperature. After that, the electrolyte solution was coated over an area of 2 cm × 1 cm = 2 cm^2 on the MnO$_2$@AuNF network electrode followed by drying at room temperature for 24 h in air. The uncoated area of the electrodes was then painted with silver paste as a contact point for electrochemical measurements. Finally, a flexible transparent supercapacitor device is fabricated by assembling and pressing two similar electrodes together, where the gel electrolyte acts as both the binder as well as the separator. The effective working area of the device was 4 cm^2.

Characterization

The material morphologies were examined by field emission scanning electron microscopy (FE-SEM, Zeiss EVO-50). The chemical composition of the materials was analyzed by X-ray photoelectron spectroscopy (XPS) using a Theta Probe AR-XPS system, Thermo Fisher Scientific, UK, where Al Kα was used as the X-ray source at the Busan center of KBSI. Optical transmittances of the films were measured using UV-Vis-NIR spectroscopy (Jasco-ARSN-733). The sheet resistance of the samples was measured using a four-point-probe surface resistivity meter (MSTEC), with a Keithley-2182A nanovoltmeter interfaced with a Keithley-6221 DC/AC current source. The bending test was performed using a Radius Bending Tester-JIRBT-610. The electrochemical performance of the core–shell MnO$_2$@AuNF network electrode and fabricated supercapacitor device was investigated in three and two-electrode configurations, respectively using a Zive sp^2 electrochemical workstation (WonATech).

Results and discussion

The fabrication process of the core–shell MnO$_2$@AuNF network electrode is illustrated in the schematic diagram, Fig. 1. In the proposed technique, firstly, a junction-less, highly conductive free-standing gold coated PVA nanofiber network (AuNF network) was fabricated using a conventional electrospinning process and thermal vacuum deposition technique.[46] The obtained free-standing AuNF network was then transferred onto a flexible polymer PEN (polyethylene naphthalate) substrate followed by dropping IPA solution over the network and drying at 50 °C for 30 min in an oven. Secondly, an electrochemically active MnO$_2$ nanosheet was electrodeposited over the AuNF network on a PEN substrate using potentiostatic

electrodeposition technique, forming a core–shell structure of the MnO$_2$@AuNF network.

The surface morphologies of the AuNF network and core–shell MnO$_2$@AuNF network electrodes were characterized by field emission scanning electron microscopy (FE-SEM). The surface FE-SEM photograph of the AuNF network reveals the uniform distribution of AuNFs over the large area with average diameters of ∼300 to 350 nm, determined from the FE-SEM image (Fig. S1, ESI†). Also, AuNFs in the network were naturally interconnected at each junction to form a seamless network structure, as seen in Fig. 2b, a magnified FE-SEM photograph of Fig. 2a (Fig. S1, ESI†), and thus might boost the electrical conductivity of the electrode. Fig. 2c shows the magnified cross-sectional FE-SEM photograph of a single AuNF, confirming the formation of the AuNF structure. Fig. 2d shows the low magnification surface FE-SEM photograph of the electrodeposited core–shell MnO$_2$@AuNF network on the PEN substrate. The photographs show that the MnO$_2$ nanosheets were uniformly deposited on the AuNF network, forming a uniform core–shell structure of the MnO$_2$@AuNF network (Fig. S2, ESI†). High-magnification FE-SEM (Fig. 2e) provided further evidence of the formation of a spiky MnO$_2$ nanosheet (inset Fig. 2e, S2, ESI†), and the magnified cross-sectional FE-SEM photograph (Fig. 2f) demonstrated the encapsulation of AuNFs by MnO$_2$, resulting in a core–shell nanofiber network structure. From the FE-SEM photograph, the average diameters of the MnO$_2$@AuNFs were found to be in the range of ∼1 to 2 μm, suggesting an increase in the diameter of the nanofibers after electrodeposition of MnO$_2$ on the AuNFs (Fig. S1, ESI†). The thin porous and highly interconnected spiky nanosheet structure is known to enhance the surface area, electrolyte ion diffusion rate and finally the overall electrochemical performance of the electrode materials.[17,33] Energy dispersive spectroscopy (EDS) was also performed to investigate the elemental distribution of the electrodeposited MnO$_2$ nanosheets on the AuNF network. In Fig. 2g, the EDS mapping image of the MnO$_2$@AuNF network showed the uniform distribution of Mn, O, and Au elements throughout the whole AuNF area. Also, the EDS mapping image of the AuNF network showed a uniform distribution of Au over the PVA-NF network (Fig. S3, ESI†).
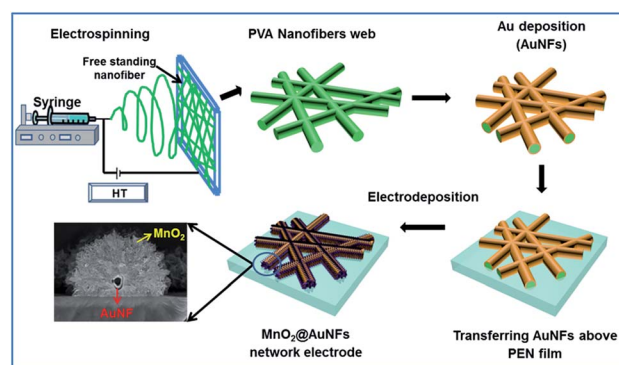

Fig. 1 Schematic diagram for the fabrication of core−shell MnO$_2$@-AuNF network electrodes using a scalable electrospinning process.
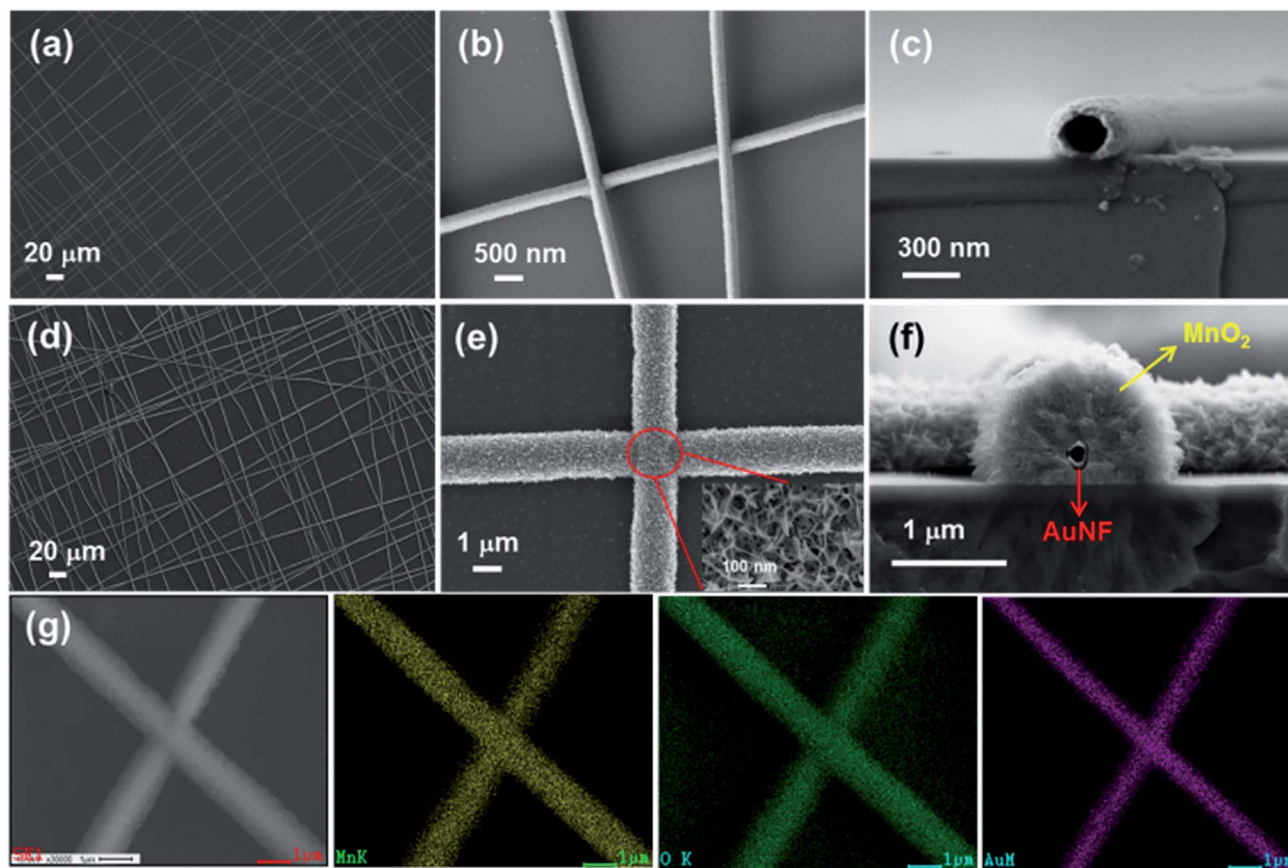
Fig. 2 (a) FE-SEM photograph of the AuNF network electrode on the PEN substrate. (b) Magnified FE-SEM photograph of the AuNF network showing fused structure AuNFs at their respective junctions. (c) Magnified cross-sectional FE-SEM photograph of a AuNF structure. (d) Surface FE-SEM photograph of the electrodeposited core–shell MnO_2@AuNF network electrode on the PEN substrate. (e) Magnified FE-SEM photograph of the MnO_2@AuNF network (inset: high resolution magnified FE-SEM image of the MnO_2 nanosheets deposited on AuNFs). (f) Cross-sectional magnified FE-SEM image of core–shell MnO_2@AuNFs, confirming the formation of a core–shell structure. (g) EDS mapping of the core–shell MnO_2@AuNF network electrode, demonstrating the uniform distribution of MnO_2 over the AuNF network.

The chemical composition of the electrodeposited core–shell MnO_2@AuNF network electrode was analyzed using X-ray photoelectron spectroscopy (XPS). Fig. 3a shows the XPS survey spectrum of the core–shell MnO_2@AuNF network electrode on a PEN substrate which indicated the presence of Mn, O, C and Au as its constituent elements corroborating the EDS results. The presence of carbon might come from the PEN substrate, as the MnO_2@AuNF network leaves large open areas of the PEN substrate. The high-resolution XPS spectrum of Mn 2p, Fig. 3b shows two peaks located at 642.1 and 653.7 eV corresponding to Mn $2p_{3/2}$ and Mn $2p_{1/2}$ electrons, respectively, which demonstrate the presence of Mn^{4+} in the obtained MnO_2 nanosheet structure. Furthermore, the binding energies of Mn $2p_{3/2}$ and Mn $2p_{1/2}$ show a spin-energy separation of 11.6 eV, indicating the formation of MnO_2, which agrees with earlier reported values for MnO_2.[47,48] The O 1s deconvolution shown in Fig. 3c shows three peaks at about 529.7, 531.8 and 533.4 eV, corresponding to Mn–O–Mn,[49] C=O, and C–O.[50] The presence of C=O and C–O might arise from the PEN substrate, as suggested by an earlier report.[50] Fig. 3d shows the XPS spectrum of Au 4f, with two peaks located at 83.04 and 86.87 eV corresponding to Au $4f_{7/2}$ and Au $4f_{5/2}$
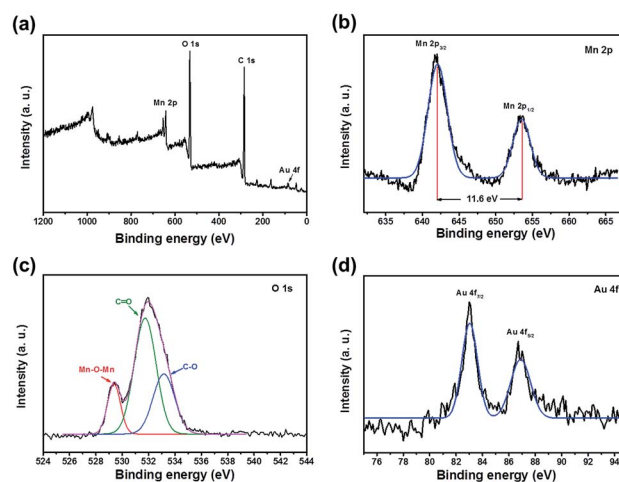

Fig. 3 XPS spectra of (a) survey scan, (b) Mn 2p (c) O 1s, and (d) Au 4f.

electrons, respectively, with a spin-energy of separation of 3.8 eV.[51] The binding energy of the Au 4f was found to be shifted towards the lower energy (83.04 eV) compared to that of pure Au

nanofiber network (83.74 eV) (Fig. S4, ESI†), indicating a strong interaction between AuNFs and the MnO_2.[52,53] Therefore, the above SEM, EDS, and XPS results prove the successful synthesis of the MnO_2 nanosheet on AuNFs and their uniform distribution throughout the AuNF network.

Fig. 4a shows the optical transmittance spectra of the AuNF network and electrodeposited core–shell MnO_2@AuNF (9 min) network electrodes on a PEN substrate. The AuNF network electrode on a PEN substrate showed a transmittance of ~93.13% with a sheet resistance of 9.58 Ω sq^{-1}. A decrease in the optical transparency of the MnO_2@AuNF network electrode was observed with an increase in the electrodeposition time (Fig. S5a, ESI†). This decrease in optical transparency with increasing electrodeposition time might be due to the increase in the thickness of the electrodeposited MnO_2 with time which increases the overall nanofiber diameter as observed in the FE-SEM photograph (Fig. 2e). This, in turn, increases the surface coverage area of the NF network electrode. It also could have been due to the dark/black colour of MnO_2 and a digital photograph of the MnO_2@AuNF network electrode at various electrodeposition times is shown in Fig. S5b, ESI†. Optical transmittance losses of ~8% (~86% T) and 16% (~77% T) were observed at 9 min and 15 min of electrodeposition time respectively, for the MnO_2@AuNF network electrode, compared to the bare AuNF network electrode. The high transparency of the core–shell MnO_2@AuNF network electrode might be due to the selective electrodeposition of MnO_2 over only the AuNF network, forming a core–shell MnO_2@AuNF network structure which results in a large open area, as depicted by the FE-SEM image in Fig. 2d. Fig. 4b shows the digital photographs of a bare PEN substrate in comparison with the AuNFs/PEN network

electrode before and after electrodeposition of MnO_2, demonstrating the high transparency of both electrodes (easily seen the text behind the electrodes), where the MnO_2@AuNF electrode showed a little bit darker color compared to the AuNF network electrode. Again, the electromechanical properties of the AuNF network and MnO_2@AuNF network electrodes on a PEN substrate were characterized by measuring the electrical resistance of the electrodes during the mechanical bending process. Fig. 4c shows a comparison of the changes in the resistance of the electrodes as a function of the bending radius for the bare AuNF network and MnO_2@AuNF network (9 min) electrodes. It is quite significant that both the samples showed almost a constant resistance value even after bending up to a radius of 3 mm (Fig. 4c), but a slight increase in the resistance was observed after bending to a radius of 2.0 mm with a ~6% increase in resistance at the 1.0 mm bending radius (inset Fig. 4c). Moreover, the electrodes also showed excellent bending fatigue strength; the resistance of the electrode showed only a ~5% increase in resistance (inset Fig. 4d), even after 10 000 repeated bending cycles at a 3.0 mm bending radius (Fig. 4d). The high electro-mechanical properties of the MnO_2@AuNF network electrode might be due to the high mechanical flexibility of the core AuNF network along with the direct growth process of MnO_2 over the AuNF network. The electro-mechanical properties of the MnO_2@AuNF network electrode were comparable or higher to those of the earlier reported metal network/grid electrodes fabricated by other techniques.[28,34,42,54–56]

Next, the electrochemical properties of the MnO_2@AuNF network electrodes were investigated by cyclic voltammograms (CVs), using a three-electrode configuration where the MnO_2@AuNF network electrode was used as the working electrode, and platinum wire and Ag/AgCl as the counter and reference electrodes, respectively. The CV curves of the MnO_2@AuNF network electrode were recorded at different scan rates in the 1 M Na_2SO_4 electrolyte at room temperature. From the above optical characterization, the electrodeposition times of MnO_2 on the AuNF network showed a strong effect on the optical transparency of the electrode, and so, might also have a strong effect on the electrochemical properties of the MnO_2@AuNF network electrode. Thus, the relationship between the electrodeposition time of MnO_2 on the AuNF network with the optical and electrochemical properties was examined. The comparison of the CV curves of MnO_2@AuNF network electrodes at a scan rate of 50 mV s^{-1} with different MnO_2 electrodeposition times is shown in Fig. S6a and b, ESI.† It was evident that the current density, along with CV loop areas of the electrode increased steadily with the increase in MnO_2 electrodeposition time, suggesting an increase in areal capacitance of the electrode, while the optical transmittance of the electrode decreased (Fig. S5, ESI†). The increase in capacitance with electrodeposition time was obvious as MnO_2 nanosheets over the AuNFs became obviously denser and bigger with the increase in electrodeposition times, which in turn increased the active surface area of the MnO_2@AuNF network electrode as evident in Fig. S2, ESI†.[17,32,33] Thus, the specific capacitance might be improved by increasing the MnO_2 deposition time
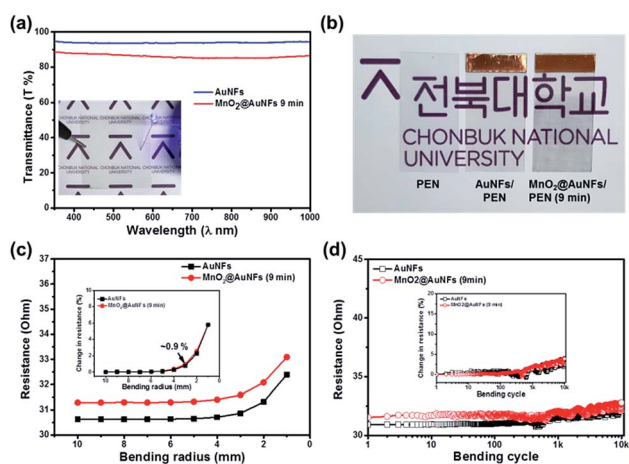

Fig. 4 (a) Optical transmittance spectra of the AuNF network electrode and MnO_2@AuNF network electrode (inset: digital photographs of a 5 × 5 cm^2 AuNF network electrode on the PEN substrate lighting a blue LED lamp). (b) Digital photograph of the bare PEN substrate in comparison with the AuNFs/PEN network electrode before and after MnO_2 electrodeposition (9 min), indicating high transparency of both electrodes. (c) Change in resistance of the AuNF electrode and MnO_2@AuNF electrode with the bending radius (inset: percentage change in resistance). (d) Change in resistance of the electrodes with a bending cycle (inset: percentage change in resistance with cycle).

10676 | J. Mater. Chem. A, 2019, 7, 10672–10683

This journal is © The Royal Society of Chemistry 2019

over the AuNF network. However, larger MnO_2 mass loading networks will eventually lead to a decrease in the optical transparency of the electrode, as described in the above section. Fig. S6c, ESI† illustrates the graph of the areal capacitance and optical transmittance as a function of the MnO_2 electrodeposition time on the AuNF network electrode. It is observed that with increasing the electrodeposition time of the MnO_2, the areal capacitance of the electrode increases sharply up to a maximum limit of 10.22 mF cm^{-2} at a scan rate of 50 mV s^{-1} for 25 min deposition time. Further increase in the electrodeposition time leads to a decrease in the areal capacitance as well as the optical transmittance of the electrode. However, to produce a high-performance transparent supercapacitor, the material should have both high optical transparency and excellent electrochemical properties. So, from the above experimental results, MnO_2@AuNF electrode prepared with 9 min electrodeposition time exhibiting an areal capacitance of 5.46 mF cm^{-2} and optical transmittance ~86% is considered to be the optimized sample and is used for further electrochemical analyses.

CV curves of the MnO_2@AuNF network electrode in a potential window of 0–0.8 V, *versus* an Ag/AgCl reference electrode measured at various scan rates from 5 to 200 mV s^{-1} showed a quasi-rectangular shape, demonstrating excellent charge storage characteristics of the MnO_2@AuNF network electrode (Fig. 5a). To check any contribution of the AuNF network to the large CV curve of the MnO_2@AuNF network electrode, the CV curves of the bare AuNF network electrode was also studied and is shown in Fig. S7a, ESI†. It is important to note that the bare AuNF network electrode showed an extremely low current density suggesting its negligible contribution towards the large CV response of the MnO_2@AuNF network electrode. This confirms that the large CV curve is solely from the MnO_2 nanosheets of the core–shell MnO_2@AuNF electrodes. The galvanostatic charge/discharge (GCD) measurement was performed at a potential window of 0–0.8 V with varying current densities ranging from 0.02 mA cm^{-2} to 0.25 mA cm^{-2} (Fig. 5b). The GCD curves showed that at different current densities, the electrode displayed nearly symmetric triangular shapes, indicating excellent electrochemical capacitive characteristics and reversible faradaic reactions between Na^+ ions in the electrolyte and the MnO_2 nanosheets.[57,58] Similar triangular shaped GCD curves were also observed for the samples of different electrodeposition times (Fig. S6d, ESI†). The areal capacitance (mF cm^{-2}) of the electrodes was calculated from the CV curve (ESI†) and is shown as a function of scan rate in Fig. 5c. The areal capacitance of the electrode was found to be 8.26 mF cm^{-2} at a scan rate of 5 mV s^{-1}, which decreased to only 4.86 mF cm^{-2} when the scan rate was increased to 100 mV s^{-1}, indicating good rate performance of the electrode. The volumetric specific capacitance of the MnO_2@AuNF network electrode was also calculated and found to be 24.5 F cm^{-3} at a current density of 0.01 mA cm^{-2}. The calculated specific volumetric energy density and the corresponding power density of the MnO_2@AuNF network electrode were found to be 3.47 mW h cm^{-3} (energy density) at a power density of 0.03 W cm^{-3}, and 1.61 mW h cm^{-3} (energy density) at a power density of 1.25

W cm^{-3}, respectively. The electrochemical performance of the core–shell MnO_2@AuNF network electrode was superior to many reported transparent flexible supercapacitor electrodes, such as graphene,[10] MnO_2/ITO/PET,[32] Ag–Au core–shell nanowires,[59] metal nanowires/PEDOT:PSS,[27] metal nanowires/metal oxide,[34] PEDOT:PSS/metal grid,[28] metal network/MnO_2,[33] Au@MnO_2,[31] carbon nanocups[60] *etc.* These high electrochemical properties of the core–shell MnO_2@AuNF network electrode might be attributed to the advantages of the unique properties of the core AuNFs, uniform MnO_2 shell and the synergistic effect of the core–shell structure. The highly dense small sized AuNF network electrode acts as an excellent current collector and also serves as a backbone for the growth of electrochemically active MnO_2 shells throughout the entire core Au nanofibers resulting in a highly dense MnO_2@Au NF core–shell network electrode structure. The existence of high density interspaced porous MnO_2@Au nanofibers with a small period would allow the deposited shell MnO_2 active materials to interact more with the electrolyte facilitating the easy diffusion of ions/molecules *etc.* and thus enhanced their electrochemical performances.

The frequency responses of the MnO_2@AuNF network electrode (9 min) are also studied by electrochemical impedance spectroscopy (EIS) measurements in the frequency range from 0.01 to 100 kHz. Fig. 5d shows the Nyquist plots of the MnO_2@AuNF network electrode measured at the open-circuit potential (OCP) which showed an equivalent series resistance (ESR) of ~22.52 Ω, denoted from the intersection point on the real axis (inset of Fig. 5d). The nearly vertical straight line at the low-frequency regions in the Nyquist curve also illustrates an ideal capacitive behaviour of the electrode. The Bode plots, frequency dependent impedance, and phase angles are shown in Fig. S7b, ESI† It is observed that the material showed small impedance at the high-frequency region with a slope of ~−1 at a low frequency, demonstrating ideal capacitive behaviours of the supercapacitor device. At a low frequency, the device showed a phase angle of ~−80°, almost close to that of an ideal capacitor (−90°), which further confirmed the ideal capacitive behaviours. The capacitance response frequency for the supercapacitor device at a phase angle of −45° (ϕ_{45}) was found to be 0.55 Hz from the Bode plot (Fig. S7b, ESI†), which was equivalent to a relaxation time constant ($\tau_0 = 1/f_0$) of ~1.81 s. Additionally, another critical parameter for practical application is the high charge–discharge cycling stability of the electrode material. Thus, 10 000 GCD cycles were carried out to check the charge/discharge cycling stability of the electrode, at an applied current density of 75 μA cm^{-2} (Fig. 5e). The coulombic efficiency was estimated to be 100% during the entire charge–discharge cycle. The MnO_2@AuNF network electrode only showed ~6% decay in areal capacitance, *i.e.*, ~94% capacitance retention, after 10 000 GCD cycles, demonstrating excellent charge–discharge stability of the electrode material. The good cycling stability of the electrode might be attributed to the hierarchical nanosheet structure of the direct growth MnO_2 over the highly conductive AuNF network electrode. The porous structure of the MnO_2 nanosheets on the AuNF network electrode might offer a large specific surface, which in turn can provide more active
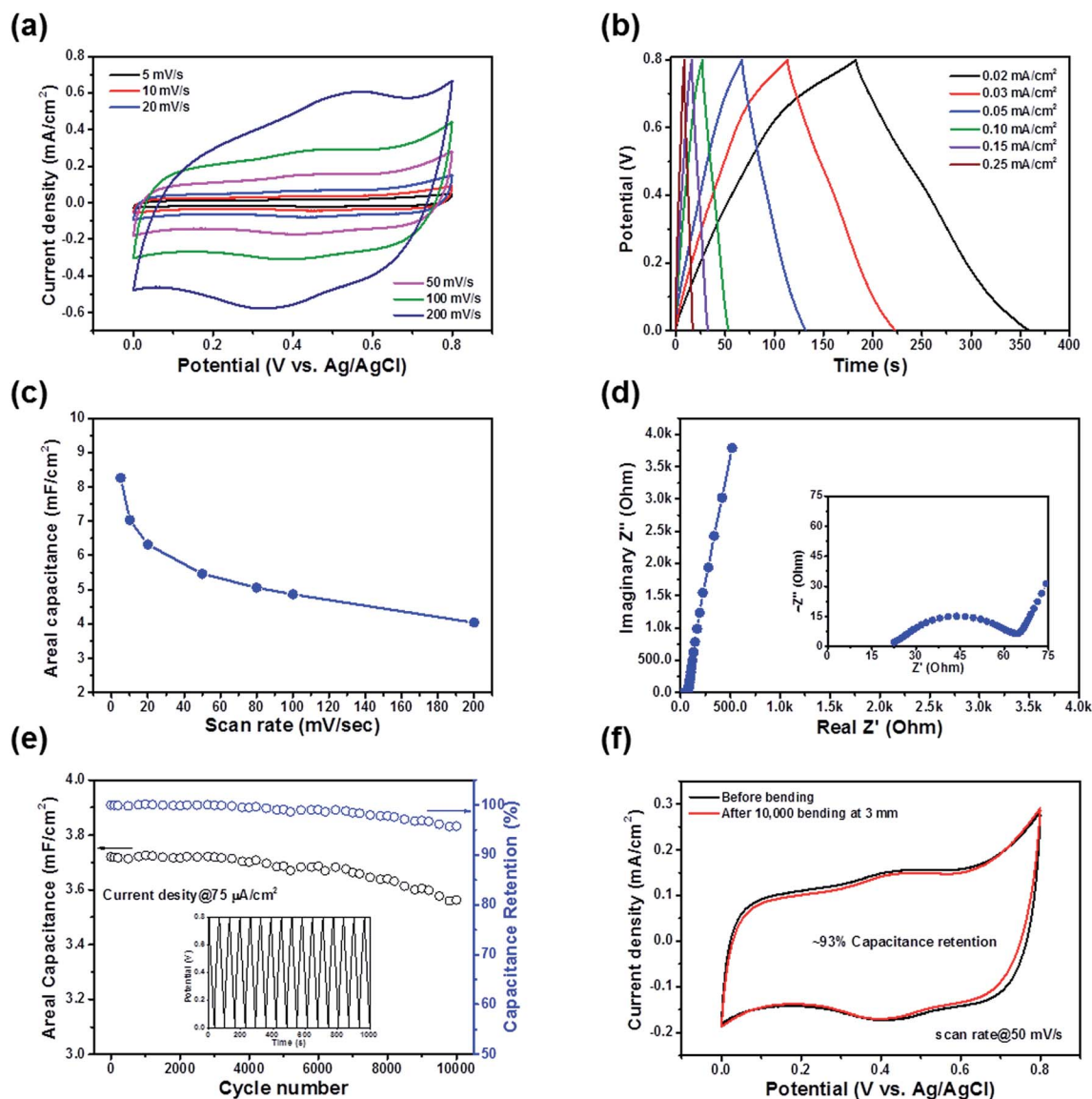
This journal is © The Royal Society of Chemistry 2019

J. Mater. Chem. A, 2019, 7, 10672–10683 | **10677**

Fig. 5 Electrochemical measurements of the core–shell MnO$_2$@AuNF network electrode (9 min) in a three-electrode configuration in 1 M Na$_2$SO$_4$ electrolyte. (a) CV curves of the electrode at different scan rates from 5–200 mV s^{-1}. (b) GCD curves of the electrode at different applied current densities. (c) Change in areal capacitance (C/A) as a function of scan rate mV s^{-1} determined from the CV curves in a. (d) Imaginary Z'' vs. real Z' Nyquist plots of the electrode in the frequency range of 0.01 to 100 kHz. (e) Cyclic stability of the MnO$_2$@AuNFs network electrode at 75 mA cm^{-2} current density, showing ∼95% capacitance retention. (f) Comparison of the CV curves of the MnO$_2$@AuNF network electrode before and after 10 000 repeated bending cycles at a scan rate of 50 mV s^{-1}.

redox sites to enable the quick passage of electrolyte ions. Again, the highly conductive nature of the AuNF network electrode could enhance the conductivity of the MnO$_2$ nanosheets and promote the fast electron transport efficiency between the AuNF network electrode and the MnO$_2$ nanosheets.[17] The electrochemical performance, along with the transparency of our MnO$_2$@AuNF network electrode was compared with previously reported flexible transparent supercapacitors (Table S1, ESI†). The electrochemical-mechanical properties of the MnO$_2$@AuNF network electrode were also investigated and are shown in Fig. 5f. The CV curves of the MnO$_2$@AuNF network electrode before and after 10 000 bending cycles at a radius of 3.0 mm (bending radius) are almost overlapped with one another with

just a ∼7% decrease in areal capacitance, demonstrating the high mechanical flexible properties of the MnO$_2$@AuNF network electrode.

Finally, we have fabricated a flexible transparent symmetric supercapacitor as a portable transparent energy storage device by assembling two MnO$_2$@AuNF network electrodes as both the positive and negative electrode, with a PVA/LiCl gel electrolyte acting as both the separator and ionic electrolyte (Fig. 6a). The fabricated supercapacitor device showed high optical transparency with ∼79% transmittance in the visible range, only a 6–7% transmittance decrease compared to the electrode, (Fig. 6b, inset: a photograph of the device attached to a pen) showing its good transparency. The high transmittance of the fabricated
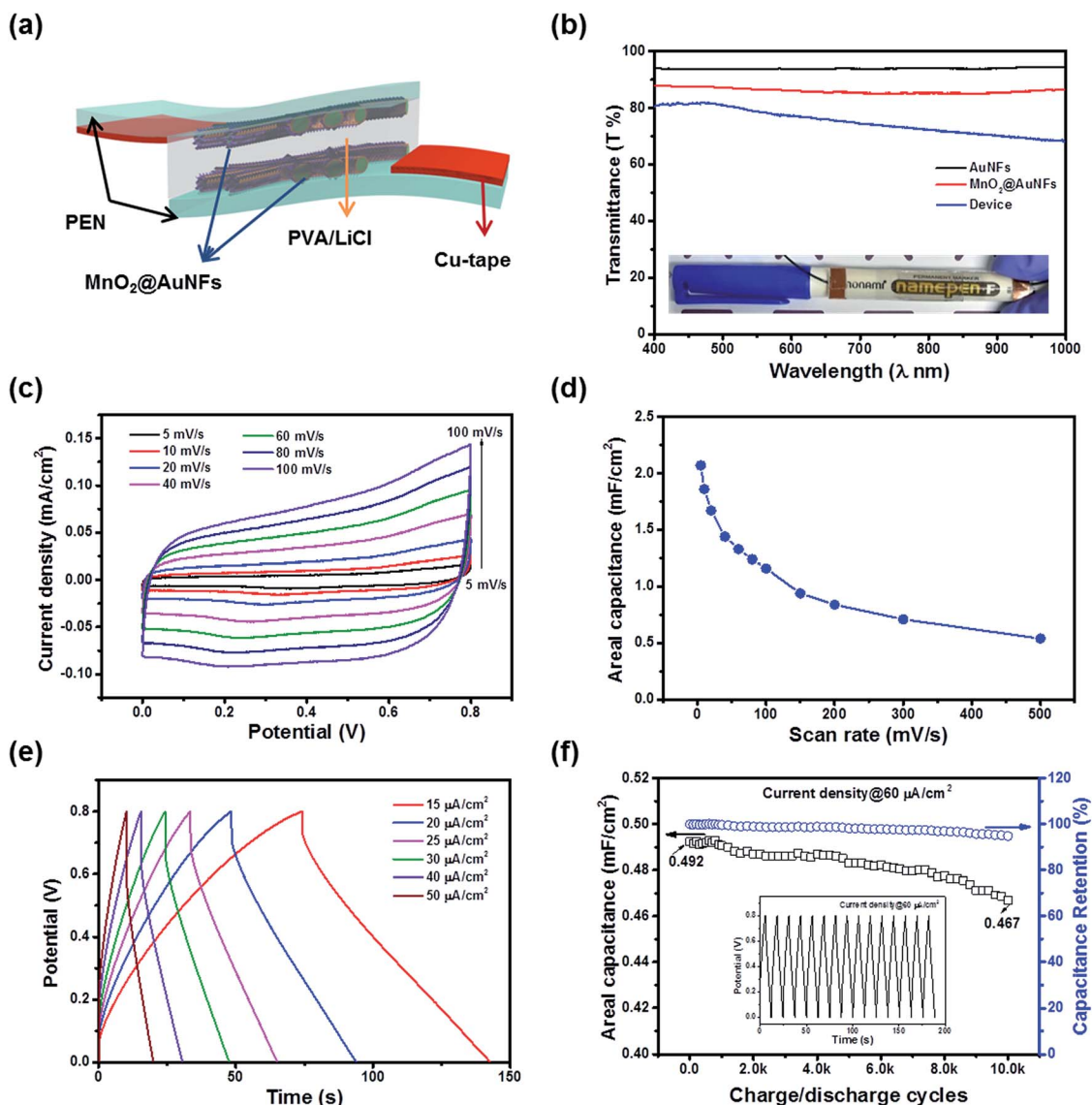
10678 | J. Mater. Chem. A, 2019, **7**, 10672–10683

This journal is © The Royal Society of Chemistry 2019

Fig. 6 (a) Schematic diagram of the symmetric supercapacitor device based on the MnO_2@AuNF network electrode. (b) Optical transmittance spectra of the AuNF network, MnO_2@AuNF network electrodes, and an assembled solid-state supercapacitor device (inset: the digital photograph of a fabricated supercapacitor device attached to a color pen). (c) CV curves of the fabricated supercapacitor device at scan rates from 5–100 mV s^{-1}. (d) Change in the areal capacitances (C/A) of the device measured from the CV curves (c) with scan rate. (e) GCD curves of the devices measured at different applied current densities. (f) Device stability tests upon repeated charging/discharging for 10 000 cycles at 60 μA cm^{-2} current density.

solid-state flexible supercapacitor device can be ascribed to the high transmittance of the MnO_2@AuNF network electrodes and the electrolyte. The digital photograph of the gel electrolyte film coated on PEN is shown in Fig. S8a, ESI,† showing its high transparency. The transparency of the device was almost comparable to or higher than those reported for transparent supercapacitors.[17,27,28,31–33] The electrochemical performance of the flexible supercapacitor devices was studied using cyclic voltammograms (CVs) using a two-electrode configuration system. Fig. 6c shows the CV curves of the flexible device in the range 0 to 0.8 V, at scan rates ranging from 5 mV s^{-1} to 100 mV s^{-1}. The supercapacitor device still retained its CV curved shape, even at a high scan rate of 1 V s^{-1}, indicating excellent

capacitive behavior and low contact resistance (Fig. S8b, ESI†). The areal capacitances (mF cm^{-2}) of the device were calculated from the CV curves and are shown in Fig. 6d as a function of scan rate. At a low scan rate of 5 mV s^{-1}, the areal capacitance of the supercapacitor device was calculated to be 2.07 mF cm^{-2}, which decreased to 1.18 mF cm^{-2} at the scan rate of 100 mV s^{-1}. The GCD curve of the flexible device measured with a potential window of 0 to 0.8 V under different applied current densities exhibited a typical symmetric triangular shape, indicating good electrochemical capacitive characteristics (Fig. 6e). The symmetric charge/discharge curves of the device also indicated a relatively high coulombic efficiency. It is important to note that the lifetime performance of a device is determined by the

This journal is © The Royal Society of Chemistry 2019

J. Mater. Chem. A, 2019, 7, 10672–10683 | 10679

repeated charge/discharge cycle stability for practical applications. Fig. 6f shows the charge/discharge cycle stability of the device, determined by carrying out 10 000 GCD cycles at an applied current density of 60 μA cm^{-2}. The cycling stability of our solid-state device was also found to be excellent. The device retained ~94% of its initial capacitance, *i.e.*, ~6% decay in areal capacitance after 10 000 continuous charge/discharge cycles, signifying high cycling stability of the device. The small decrease in the capacitance value after 10 000 cycles might be due to the dissolution/loss of a small proportion of MnO$_2$ caused by volume expansion of MnO$_2$ during repeated charge–discharge cycles.[61–63] The frequency response curves of the

fabricated devices were also examined by electrochemical impedance spectroscopy (EIS) measurements from 100 kHz to 0.1 Hz (Fig. S8d, ESI†). Nyquist plots measured at the open-circuit potential (OCP) illustrated an equivalent series resistance (ESR) of ~41.11 Ω. In the low-frequency regions, the device exhibited a nearly vertical straight line which was almost parallel to the imaginary axis, demonstrating an ideal capacitive behaviour. Also, the presence of a small semi-circle-like response in the high-frequency regions indicated high ionic conductivity at the electrode/electrolyte interfaces.

The mechanical flexibility of the device was also investigated by measuring the electrochemical performance of the device
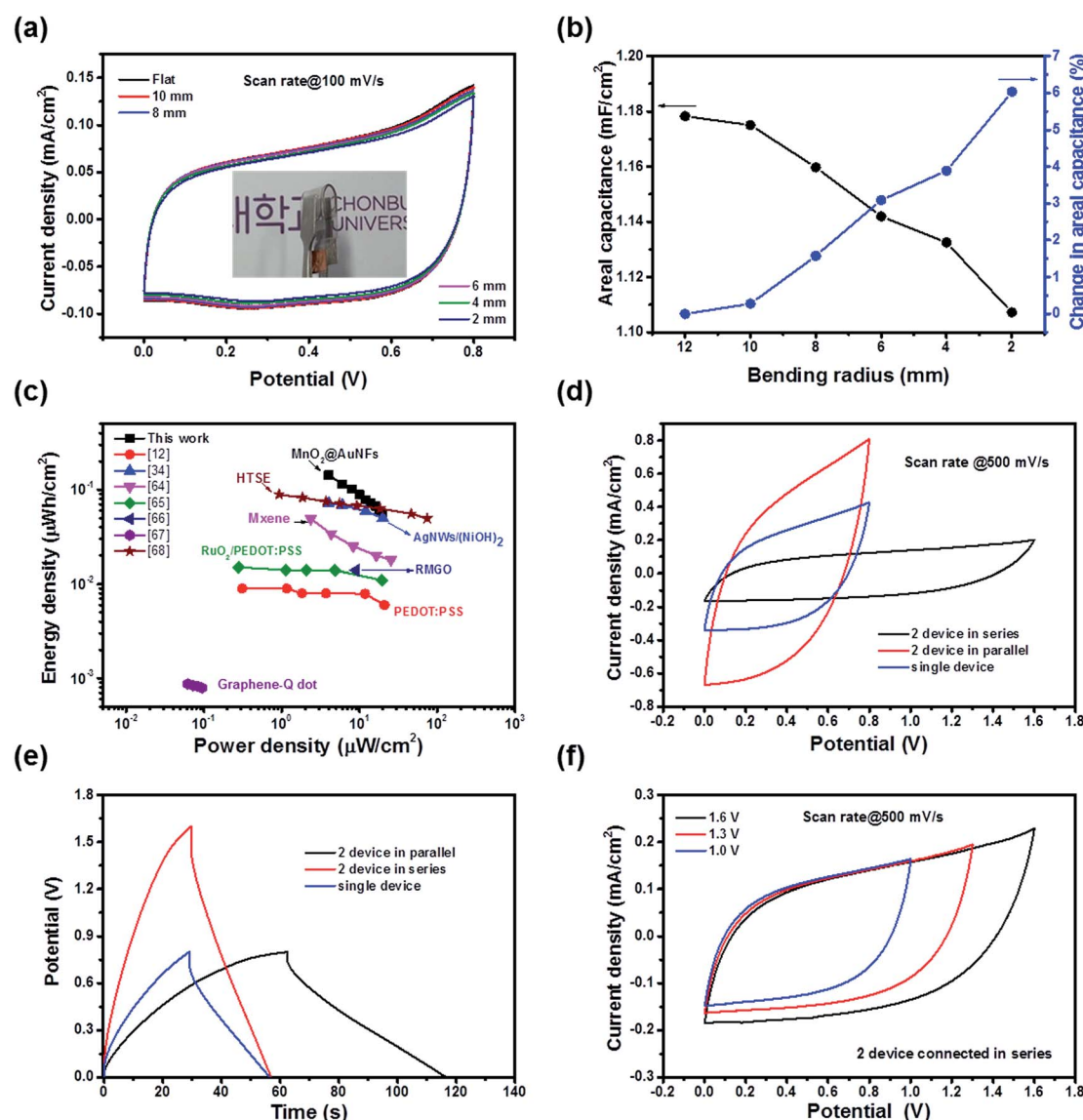

Fig. 7 (a) CV curves of the flexible supercapacitor device measured at a scan rate of 100 mV s^{-1} under different mechanical bending radii (inset: digital photograph of flexible device showing its bending capability). (b) The measured areal capacitances (C/A) and corresponding change in areal capacitance (%) with respect to different mechanical bending radii. (c) Ragone plots (energy density *vs.* power density) of the flexible transparent supercapacitor device based on a MnO$_2$@AuNF network electrode, compared to previously reported flexible transparent supercapacitor devices. (d) CV curves measured at a scan rate of 500 mV s^{-1} for a single device, two in series, and two in parallel configuration. (e) GCD curves for a single device, two devices in series, and in parallel configuration. (f) CV curves of two devices connected in series at three different potential windows at a scan rate of 500 mV s^{-1}.

under different mechanical bending radii. The device demonstrated excellent mechanical bending characteristics, as shown in Fig. 7a, (Fig. S9c, ESI†). The CV curves of the device at the bending radii of 10, 8, 6, 4 and 2 mm, were measured at a scan rate of 100 mV s^{-1}. The calculated normalized areal capacitances determined from the CV curves in Fig. 7a were plotted against the bending radius (Fig. 7b). From the mechanical bending tests, the calculated capacitance value was observed to decrease from 1.18 mF cm^{-2} to 1.11 mF cm^{-2} as the bending radius was decreased from 10 mm to 2 mm, with a maximum change of ~6 percent. After bending to a radius of 2 mm, EIS measurement of the device was again performed in the same frequency range (100 kHz to 0.1 Hz) to confirm the mechanical stability of our device, as shown in Fig. S8d, ESI.†. It was observed that there was a slight increase in the equivalent series resistance of the device from 41.11 to 42.95 Ω, and an almost similar vertical line with a steep decrease in the slope which indicated a nearly ideal capacitive behaviour of the device even after bending. The mechanical flexibility of our supercapacitor device was comparable to the earlier reported flexible transparent supercapacitors.[17,27,28,31–33] Table S1, ESI† summarizes the comparison of transparency and electrochemical features of our device with other flexible transparent supercapacitors. Our device showed excellent electrochemical performance at high transparency with good mechanical bending properties. Fig. 7c shows the energy densities *vs.* power densities graph (Ragone plot) in comparison with other earlier reported transparent supercapacitor devices. The comparison of the energy densities and power densities of the flexible transparent supercapacitor device with that of other reported transparent supercapacitor devices is also shown in Table S2, ESI.† Our MnO$_2$@AuNF network electrode-based symmetric solid state transparent supercapacitor device showed an energy density of 0.14 μW h cm^{-2} at a power density of 4 μW cm^{-2}, and 0.05 μW h cm^{-2} at a power density of 20 μW cm^{-2}, and outperformed previously reported transparent supercapacitor devices, such as PEDOT:PSS,[12] AgNWs/Ni(OH)$_2$/PEDOT:PSS,[34] MXene,[64] RuO$_2$/PEDOT:PSS,[65] reduced multilayer graphene oxide thin films,[66] graphene quantum-dot[67] and HTSE.[68] Our device performance, an energy density of 0.14 μW h cm^{-2} at a power density of 4 μW cm^{-2} was enough to store energy from a nanogenerator device.[69] Though the device displayed high areal capacitance as described above, it still stored very low energy, which might make it unsuitable for real practical applications. To achieve the required specific capacitance or voltage (energy and power), the supercapacitor devices could either be connected in parallel, in series, or both, according to the specific application.[70] The comparison of the CV curves of a single device, two devices connected in parallel, and in series configurations are shown in Fig. 7d. As evident from Fig. 7d, the operating potential window for a single device can be extended from 0.8 V to 1.6 V for a tandem device by connecting two devices in series, while an output current density twice the value of a single device (*i.e.*, a capacitance value almost twice that of a single device) can be achieved by simply connecting two devices in parallel. Also, from the GCD curves in Fig. 7e, it was observed that the

operating voltage could be extended from 0.8 V for a single device to 1.6 V by connecting two devices in series. Fig. 7f shows the CV curves of the two devices connected in series with respect to different window potentials of 1.0 V, 1.3 V, and 1.6 V at a scan rate of 500 mV s^{-1}. The series device configuration illustrated close to ideal rectangular curves, even at a high scan rate of 500 mV s^{-1}, with an extended window potential up to 1.6 V and can power a RED LED lamp (Fig. S9c, ESI†). The above results suggest that our core–shell MnO$_2$@-AuNF network electrode-based device holds promise for practical applications as a transparent flexible portable power source for transparent electronic gadgets. Thus, the electro-deposited nanosheet core–shell MnO$_2$@AuNF network electrodes could be excellent electrodes for future flexible transparent energy storage device applications because of their high transparency with excellent electrochemical-mechanical performance. In our study, we chose Au metal, though it is expensive, because of its stability in electro-chemical reactions where other metals, such as Cu and Ag fail. So, future investigations may be undertaken to replace expensive Au metals with other inexpensive metals or alloys.

Conclusions

In conclusion, a novel technique was proposed to fabricate metal-oxide@metal nanofiber network structures for flexible transparent supercapacitors, using scalable electrospinning, thermal vacuum deposition, and electrodeposition techniques. A highly-conducting, transparent AuNF network electrode was first fabricated using an electrospun nanofiber template with a thermal vacuum deposition of Au metal. The fabricated AuNF network electrode possessed high electro-optical properties, with a sheet resistance of 9.58 Ω sq^{-1} at a transparency of ~93.13 percent (%). Utilizing a simple electrodeposition technique, a hierarchal MnO$_2$ nanosheet was deposited over the AuNF network, yielding a highly-interconnected core–shell MnO$_2$@AuNF network electrode structure with AuNFs as the current collectors. The transparency and electrochemical performance of the core–shell MnO$_2$@AuNF network electrode could be simply tailored by controlling the electrodeposition time. The MnO$_2$@AuNF network electrode demonstrated a high areal capacitance of 8.26 mF cm^{-2} at 5 mV s^{-1}, along with high transparency (~86%), high rate capability, long-term cyclic stability, and excellent mechanical flexibility. Additionally, the assembled flexible transparent supercapacitor device showed high transparency (~79%), a high areal capacitance of 2.07 mF cm^{-2} at 5 mV s^{-1}, and high energy density of 0.14 μW h cm^{-2} at a power density of 4 μW cm^{-2}. The device also showed a long charge/discharge cycle stability and good mechanical bending properties. With the AuNF network electrode as a current collector and application of the electrode-position technique, various transition-metal oxides, such as RuO$_2$, NiO, Co$_3$O$_4$ *etc.* core–shell network electrode structures might also be fabricated.

Conflicts of interest

There are no conflicts to declare.

This journal is © The Royal Society of Chemistry 2019

J. Mater. Chem. A, 2019, **7**, 10672–10683 | **10681**

Acknowledgements

Notes and references

1 S. De, P. E. Lyons, S. Sorel, E. M. Doherty, P. J. King, W. J. Blau, P. N. Nirmalraj, J. J. Boland, V. Scardaci, J. Joimel and J. N. Coleman, *ACS Nano*, 2009, **3**, 714.

2 H.-Z. Geng, K. K. Kim, K. P. So, Y. S. Lee, Y. Chang and Y. H. Lee, *J. Am. Chem. Soc.*, 2007, **129**, 7758.

3 G. Eda, Y. Lin, S. Miller, C. Chen, W. Su, M. Chhowalla, G. Eda, Y. Lin, S. Miller, C. Chen and W. Su, *Appl. Phys. Lett.*, 2009, **92**, 10.

4 K. S. Kim, Y. Zhao, H. Jang, S. Y. Lee, J. M. Kim, K. S. Kim, J. H. Ahn, P. Kim, J. Y. Choi and B. H. Hong, *Nature*, 2009, **457**, 706.

5 A. Vollmer, X. L. Feng, X. Wang, L. J. Zhi, K. Mullen, N. Koch and J. P. Rabe, *Appl. Phys. A: Mater. Sci. Process.*, 2009, **94**, 1.

6 X. Wang, L. Zhi and K. Mu, *Nano Lett.*, 2008, **8**, 323.

7 T. Chen, Y. Xue, A. K. Roy and L. Dai, *ACS Nano*, 2014, **8**, 1039.

8 B. Yao, L. Huang, J. Zhang, X. Gao, J. Wu, Y. Cheng, X. Xiao, B. Wang, Y. Li and J. Zhou, *Adv. Mater.*, 2016, **28**, 6353.

9 N. Li, X. Huang, H. Zhang, Y. Li and C. Wang, *ACS Appl. Mater. Interfaces*, 2017, **9**, 9763.

10 N. Li, G. Yang, Y. Sun, H. Song, H. Cui, G. Yang and C. Wang, *Nano Lett.*, 2015, **15**, 3195–3203.

11 Y. H. Liu, J. L. Xu, S. Shen, X. L. Cai, L. Sen Chen and S. D. Wang, *J. Mater. Chem. A*, 2017, **5**, 9032–9041.

12 T. M. Higgins and J. N. Coleman, *ACS Appl. Mater. Interfaces*, 2015, **7**, 16495–16506.

13 P. Simon and Y. Gogotsi, *Nat. Mater.*, 2008, **7**, 845.

14 C. Zhang, Y. Xie, M. Zhao, A. E. Pentecost, Z. Ling, J. Wang, D. Long, L. Ling and W. Qiao, *ACS Appl. Mater. Interfaces*, 2014, **6**, 9751.

15 X. Y. Liu, Y. Q. Gao and G. W. Yang, *Nanoscale*, 2016, **8**, 4227.

16 M. A. Borysiewicz, M. Ekielski, Z. Ogorza, M. Wzorek and J. Kaczmarski, *Nanoscale*, 2017, **9**, 7577.

17 S. J. Xu, L. Chen and S. Wang, *Energy Environ. Sci.*, 2017, **10**, 2534.

18 N. Li, X. Huang, H. Zhang, Y. Li and C. Wang, *ACS Appl. Mater. Interfaces*, 2017, **9**, 9763.

19 C. S. Lee, J. E. Yoo, K. Shin, C. O. Park and J. Bae, *Phys. Status Solidi A*, 2014, **211**, 2890.

20 D. S. Hecht, L. Hu and G. Irvin, *Adv. Mater.*, 2011, **23**, 1482–1513.

21 Z. Niu, W. Zhou, J. Chen, G. Feng, H. Li and Y. Hu, *Small*, 2013, **9**, 518.

22 T. Cheng, Y. Z. Zhang, J. D. Zhang, W. Y. Lai and W. Huang, *J. Mater. Chem. A*, 2016, **4**, 10493.

23 F. Chen, P. Wan, H. Xu and X. Sun, *ACS Appl. Mater. Interfaces*, 2017, **9**, 17865.

24 K. Jo, S. Lee, S. Kim, J. Bin In, S. Lee, J. Kim, H. Lee and K. Kim, *Chem. Mater.*, 2015, **27**, 3621.

25 T. Cheng, Y. Z. Zhang, J. P. Yi, L. Yang, J. D. Zhang, W. Y. Lai and W. Huang, *J. Mater. Chem. A*, 2016, **4**, 13754.

26 J. Yu, J. Wu, H. Wang, A. Zhou, C. Huang, H. Bai and L. Li, *ACS Appl. Mater. Interfaces*, 2016, **8**, 4724.

27 X. Liu, D. Li, X. Chen, W. Lai and W. Huang, *ACS Appl. Mater. Interfaces*, 2018, **10**, 32536.

28 J. L. Xu, Y. H. Liu, Y. Gao, Y. Sun, S. Shen, X. Cai, L. Chen and S. D. Wang, *ACS Appl. Mater. Interfaces*, 2017, **9**, 27649.

29 H. Moon, H. Lee, J. Kwon, Y. D. Suh, D. K. Kim, I. Ha, J. Yeo, S. Hong and S. H. Ko, *Sci. Rep.*, 2017, **7**, 1.

30 L. Liu, Z. Niu and J. Chen, *Chem. Soc. Rev.*, 2016, **45**, 4340.

31 T. Qiu, B. Luo, M. Giersig, E. M. Akinoglu, L. Hao, X. Wang, L. Shi, M. Jin and L. Zhi, *Small*, 2014, **10**, 4136.

32 Y. Wang, W. Zhou, Q. Kang, J. Chen, Y. Li, X. Feng, D. Wang and Y. Ma, *ACS Appl. Mater. Interfaces*, 2018, **10**, 27001.

33 S. Kiruthika, C. Sow and G. U. Kulkarni, *Small*, 2017, **13**, 1701906.

34 R. Titian, M. Mayaji and J. Kang, *Nano Energy*, 2018, **53**, 650.

35 S. H. Yang, X. F. Song, P. Zhang and L. Gao, *ACS Appl. Mater. Interfaces*, 2013, **5**, 3317.

36 C. Wei, L. H. Yu, C. L. Cui, J. D. Lin, C. Wei, N. Mathews, F. W. Huo, T. Sritharan and Z. H. Xu, *Chem. Commun.*, 2014, **50**, 7885.

37 S. Park, I. Nam, G. P. Kim, J. W. Han and J. Yi, *ACS Appl. Mater. Interfaces*, 2013, **5**, 9908–9912.

38 S. Zhao, T. Liu, D. Hou, W. Zeng, B. Miao, S. Hussain, X. Peng and M. S. Javed, *Appl. Surf. Sci.*, 2015, **356**, 259–265.

39 S. Zhao, T. Liu, M. S. Javed, W. Zeng, S. Hussain, Y. Zhang and X. Peng, *Electrochim. Acta*, 2016, **191**, 716–723.

40 Z. Qiao, X. Yang, S. Yang, L. Zhang and B. Cao, *Chem. Commun.*, 2016, **52**, 7998.

41 H. Wu, L. Hu, M. W. Rowell, D. Kong, J. J. Cha, J. R. McDonough, J. Zhu, Y. Yang, M. D. McGehee and Y. Cui, *Nano Lett.*, 2010, **10**, 4242.

42 T. He, A. Xie, D. H. Reneker and Y. Zhu, *ACS Nano*, 2014, **8**, 4782.

43 K. Azuma, K. Sakajiri, H. Matsumoto, S. Kang, J. Watanabe and M. Tokita, *Mater. Lett.*, 2014, **115**, 187.

44 H. Wu, D. Kong, Z. Ruan, P.-C. Hsu, S. Wang, Z. Yu, T. J. Carney, L. Hu, S. Fan and Y. Cui, *Nat. Nanotechnol.*, 2013, **8**, 421.

45 S. An, H. S. Jo, D. Y. Kim, H. J. Lee, B. K. Ju, S. S. Al-Deyab, J. H. Ahn, Y. Qin, M. T. Swihart, A. L. Yarin and S. S. Yoon, *Adv. Mater.*, 2016, **28**, 7149.

46 S. B. Singh, Y. Hu, T. Kshetri, N. H. Kim and J. H. Lee, *J. Mater. Chem. C*, 2017, **5**, 4198.

47 Y. Zhao, P. Jiang and S. Xie, *J. Power Sources*, 2013, **239**, 393.

48 N. Yu, H. Yin, W. Zhang, Y. Liu, Z. Tang and M. Zhu, *Adv. Energy Mater.*, 2016, **6**, 1501458.

49 P. Lv, P. Zhang, Y. Feng, Y. Li and W. Feng, *Electrochim. Acta*, 2012, **78**, 515.

50 E. Gonzalez II, M. D. Barankin, P. Guschl and R. F. Hicks, *Langmuir*, 2008, **24**, 12636.

51 M. Aslam, L. Fu, M. Su, K. Vijayamohanan and V. P. Dravid, *J. Mater. Chem.*, 2004, **14**, 1795.

10682 | *J. Mater. Chem. A*, 2019, **7**, 10672–10683

This journal is © The Royal Society of Chemistry 2019

52 I. M. Arabatzis, T. Stergiopoulos, D. Andreeva, S. Kitova, S. G. Neophytides and P. Falaras, *J. Catal.*, 2003, **220**, 127–135.

53 X. Lang, A. Hirata, T. Fujita and M. Chen, *Nat. Nanotechnol.*, 2011, **6**, 232–236.

54 S. Hong, J. Yeo, G. Kim, D. Kim, H. Lee, J. Kwon, H. Lee, P. Lee and S. H. Ko, *ACS Nano*, 2013, **7**, 5024.

55 Y. Lee, W. Y. Jin, K. Y. Cho, J. W. Kang and J. Kim, *J. Mater. Chem. C*, 2016, **4**, 7577.

56 Y. S. Oh, D. Y. Choi and H. J. Sung, *RSC Adv.*, 2015, **5**, 64661–64668.

57 L. Chen, Z. Huang, H. Liang, Q. Guan and S. Yu, *Adv. Mater.*, 2013, **25**, 4746.

58 Z. Yang, J. Deng, X. Chen, J. Ren and H. Peng, *Angew. Chem., Int. Ed.*, 2013, **52**, 13453.

59 H. Lee, S. Hong, L. Lee, Y. D. Suh, J. Kwon, H. Moon, H. Kim, J. Yeo and S. H. Ko, *ACS Appl. Mater. Interfaces*, 2016, **8**, 15449.

60 H. Y. Jung, M. B. Karimi, M. G. Hahm, P. M. Ajayan and Y. J. Jung, *Sci. Rep.*, 2012, **2**, 1–5.

61 Q. Qu, P. Zhang, B. Wang, Y. Chen, S. Tian, Y. Wu and R. Holze, *J. Phys. Chem. C*, 2009, **113**, 14020.

62 Y. He, W. Chen, X. Li, Z. Zhang, J. Fu, C. Zhao and E. Xie, *ACS Nano*, 2013, **7**, 174.

63 Z. Lei, F. Shi and L. Lu, *ACS Appl. Mater. Interfaces*, 2012, **4**, 1058.

64 C. J. Zhang, B. Anasori, A. Seral-ascaso, S. Park, N. Mcevoy, A. Shmeliov, G. S. Duesberg, J. N. Coleman, Y. Gogotsi and V. Nicolosi, *Adv. Mater.*, 2017, **29**, 1702678.

65 C. John Zhang, T. M. Higgins, S. H. Park, S. E. O'Brien, D. Long, J. N. Coleman and V. Nicolosi, *Nano Energy*, 2016, **28**, 495.

66 J. J. Yoo, K. Balakrishnan, J. Huang, V. Meunier, B. G. Sumpter, A. Srivastava, M. Conway, A. L. Mohana Reddy, J. Yu, R. Vajtai and P. M. Ajayan, *Nano Lett.*, 2011, **11**, 1423.

67 K. Lee, H. Lee, Y. Shin, Y. Yoon, D. Kim and H. Lee, *Nano Energy*, 2016, **26**, 746.

68 S. Bobby, T. Kshetri, T. Ibomcha, N. H. Kim and J. H. Lee, *Chem. Eng. J.*, 2019, **359**, 197.

69 N. Thambi and A. M. Sastry, *Smart Mater. Struct.*, 2008, **17**, 043001.

70 N. Kurra, M. K. Hota and H. N. Alshareef, *Nano Energy*, 2015, **13**, 500–508.

This journal is © The Royal Society of Chemistry 2019

J. Mater. Chem. A, 2019, **7**, 10672–10683 | **10683**